Far-field shock noise prediction on the ACAT1 fan stage using a CFD/CAA chaining strategy

Majd Daroukh, Cyril Polacsek, Johan Thisse, Thomas Nodé-Langlois

FAR-FIELD SHOCK NOISE PREDICTION ON THE ACAT1 FAN STAGE USING A CFD/CAA CHAINING STRATEGY

Majd Daroukh, Cyril Polacsek
DAAA, ONERA, Université Paris Saclay, F-92322 Châtillon, France
e-mail: majd.daroukh@onera.fr
Johan Thisse, Thomas Nodé-Langlois
Airbus Operations, 31300 Toulouse, France

At take-off conditions, if the relative tip Mach number is above unity, one of the main contributor to aircraft noise is the shock noise generated by the transonic fan blades. The purpose of this paper is to propose and validate a numerical methodology for predicting this noise mechanism. The evaluation is done on the ACAT1 fan stage for which an extensive measurement campaign was conducted at the Universal Fan Facility for Acoustics rig of AneCom AeroTest GmbH (Wildau, Germany) during the TurboNoiseBB European project. A computational fluid dynamics (CFD) simulation is first performed to capture the generation of shock waves in the vicinity of the fan (assuming fully identical blades). Then, a computational aeroacoustics (CAA) simulation is realized to predict the shock wave propagation up to the near-field, with specification of the initial shock extracted from CFD in terms of conservative variables using a non-reflecting boundary condition. This chaining strategy is evaluated in different contexts (steady and unsteady simulations of the Euler or the Reynolds-averaged Navier-Stokes equations). To this end, analyses of the in-duct acoustic field at blade passing frequencies are provided and are compared with the original CFD data. Far-field acoustic radiation from the intake obtained by means of a Kirchhoff integral and using the CAA near-field solution is then evaluated against the measurements. The results highlight the effect of viscosity on the propagation and show a good behaviour of the chaining methodology in the steady and unsteady contexts.
Keywords: Fan noise, shock noise, CFD/CAA chaining method, ACAT1 fan stage

1. Introduction

During take-off and climb, the shocks emitted by the tips of the transonic fan blades highly contribute to the aircraft noise. For complex geometries and flows, numerical approaches are required to predict this noise source. The generation and radiation of shockwaves can be estimated using a computational fluid dynamics (CFD) solver in a one-simulation approach as proposed by recent studies [1, 2]. However, the associated computational cost is generally high if the propagation and radiation of acoustic waves is meant to be correctly captured over a long distance. Most of the numerical studies are therefore based on a two-step method where the shock signature is first captured by a CFD simulation and is then propagated with a computational aeroacoustics (CAA) simulation [3, 4, 5, 6]. An additional advantage of these two-step methods is that it enables a collaborative work between the engine manufacturer (computation of fan sources) and the airframe manufacturer (propagation of known sources through the intake). This approach is chosen here using the CFD/CAA chaining strategy developed by Thisse *et al.* where the shocks are injected into the CAA domain in terms of usual conservative variables using a non-reflecting

boundary condition [7]. Up to now, this method has only been applied by solving the unsteady non-linearized Euler equations in the absolute frame for the CAA step. In this context, it has been validated on canonical cases by Thisse *et al.* [7] and has been applied on a full-scale ultra high bypass ratio engine by Daroukh *et al.* [6] to study the effects of distortion on shock wave generation and radiation.

In the present paper, we intend to further validate the methodology by considering several strategies for the CAA simulation. The exercise is done on a realistic turbofan stage using the data available on the ACAT1 fan from the TurboNoiseBB European project [8]. For the sake of limiting the computational cost, no stagger variation is included between the blades in the simulations so that the acoustic waves radiate at the blade passing frequency (BPF) and its harmonics only. As a consequence, no multiple pure tone is captured and this is to be considered for the comparison with the measurements. The axisymmetry of the configuration makes possible the resolution of the shock wave propagation in a steady context by using the well-known time-azimuthal angle analogy. The validity of the chaining strategy is therefore assessed both in the steady and unsteady contexts. The effect of viscosity on the propagation is also evaluated by solving the Reynolds-averaged Navier-Stokes (RANS) equations instead of the Euler equations. The CAA results are assessed against the original CFD data in the overlapping region and against the measurements for far-field acoustics (using the Kirchhoff integral method) .

The studied configuration is first presented in Sec. 2 and the numerical strategy is detailed in Sec. 3. The results are then presented, by first focusing on the shock signature in Sec. 4, then on in-duct acoustics in Sec. 5, and finally on far-field acoustics in Sec. 6. Sec. 7 finally adresses the main conclusions.

2. The TurboNoiseBB configuration

The TurboNoiseBB configuration relates to the Universal Fan Facility for Acoustics (UFFA) rig of AneCom AeroTest GmbH (Wildau, Germany)[1] equipped with the transonic ACAT1 fan [9, 10]. The fan is composed of 20 blades with a radius R of about 0.45 m and the distance L from the fan plane to the inlet plane is approximately 1.2 m. The current study is restricted to the nominal operating point (top of climb operating condition) where the relative tip Mach number is equal to 1.21. Among available experimental data, only the far-field acoustic results are exploited here. They have been obtained from 25 microphones equally placed over an arc of radius 18.5 m centered on the fan plane from 0 to 120 deg.

3. Numerical description

3.1 CFD simulation

The first step of the numerical methodology adopted in this study for predicting shock noise is the computation of the shock wave generation with the *elsA* solver [11] (Airbus-Safran-ONERA property). For this simulation (number #0 in Table 1), the fan and the outer and inner guide vanes are modeled by restricting the domain to the in-duct part (applying a classical semi-infinite intake approximation). Only one blade/vane passage is computed per row and the steady RANS equations are solved using a mixing plane strategy. A pseudo-time marching method with backward Euler scheme and a Roe spatial scheme with a third-order limiter in space are used. The turbulence closure is dealt with the Menter k-omega SST turbulence model. Periodic boundary conditions are specified on azimuthal boundaries, all walls are considered as hard walls and classical turbomachinery boundary conditions are used (total pressure and enthalpy at inlet, static pressure at outlet). The mesh is defined in order to propagate acoustic waves correctly up to BPF3 up to the spinner nose and totalizes 67 millions points. The high number of mesh points is due to the fact that the mesh was initially designed for rotor/stator interaction noise simulation.

[1] https://www.anecom.de/services/aerodynamic-testing/fan-noise-and-performance-test/

3.2 CAA simulation

The second step of the proposed methodology is the propagation of shock waves through a CAA simulation using the chaining strategy developed by Thisse *et al.* [7]. The CAA simulation is again performed using the *elsA* solver [11]. The simulated domain (partly) shown in Fig. 1 comprises the duct from a plane just upstream of the fan (plane P0) to the near-field. In the experimental setup, the duct ends with a conic shape equipped with absorbing walls. As the current version of the solver does not have the capability to include absorbing walls, the conic shape is modified in order to avoid any acoustic reflection in this zone. Again, only one blade passage is solved due to the axisymmetry of the configuration. Three different simulations, summarized in Table 1, are performed for this step: the first one (#1) solves the steady Euler equations in the relative frame, the second one (#2) solves the unsteady Euler equations in the absolute frame, and the last one (#3) solves the steady RANS equations (with Wilcox k-omega turbulence model) in the relative frame. For the steady simulations, the implicit backward Euler time scheme is again used while a Gear scheme with 10 sub-iterations and 240 iterations per blade passage is used for the time integration of the unsteady simulation. For all simulations, the Roe spatial scheme with van Albada limiter is chosen for the space integration. The shock signature extracted from the CFD simulation is specified in terms of conservative variables using Thompson's non-reflecting boundary condition based on 1-D characteristic equations [12]. For the unsteady simulation, the boundary data is updated at each time step via the so-called trigger capacity of the solver to account for the relative-absolute frame conversion. Non-reflecting boundary conditions are specified on far-field boundaries and periodic boundary conditions are specified on azimuthal ones. All walls are considered as frictionless except for the nacelle wall in the RANS simulation which is considered as viscous. Two meshes have been realized: one for the Euler simulations and one for the RANS simulation. Both meshes have been defined in order to propagate acoustic waves correctly up to BPF3. The nacelle wall region has then been further discretized in the RANS mesh to compute the boundary layer correctly. As a result, the single-channel mesh totalizes 124 and 139 millions points for the Euler and RANS simulations respectively.

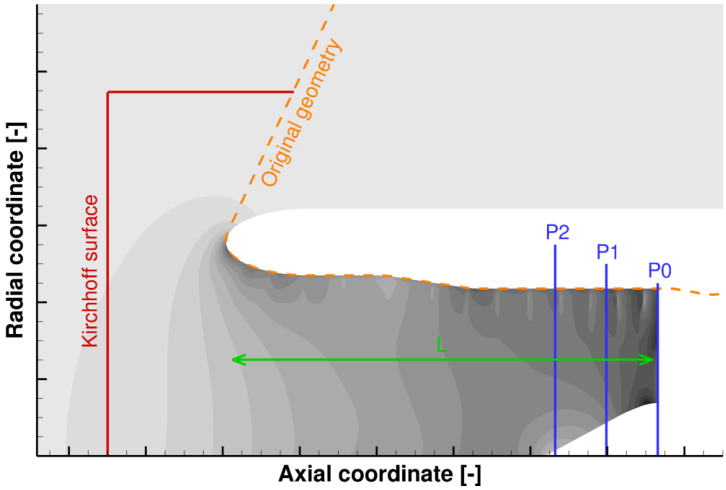

Figure 1: Computational domain of the CAA simulations and position of analysis planes.

4. Shock signature results

The capacity of the chaining methodology to correctly recover the shock signature from CFD is first evaluated. To this end, the azimuthal evolution of the fluctuating pressure over one blade passage at 95%

Table 1: Summary of performed simulations.

Number	Label	Model	Frame	Time integration	Mesh points
#0	CFD	RANS	Relative	Steady	67×10^6
#1	CAA / St. Euler	Euler	Relative	Steady	124×10^6
#2	CAA / Unst. Euler	Euler	Absolute	Unsteady	124×10^6
#3	CAA / St. RANS	RANS	Relative	Steady	139×10^6

of blade height is plotted for each simulation in Fig. 2 for the three successive axial planes P0, P1 and P2 (shown in Fig. 1). The plane P0 corresponds to the plane where the data from CFD is injected into the CAA domain, while the plane P2 is the last plane of the CFD simulation before the stretching of the mesh. On plane P0, all CAA results match the CFD ones, which proves a correct behaviour of the injection boundary condition. When going away from the injection plane, the Euler solutions start to deviate from the CFD reference. This deviation in shock angle and shock shape is similar with the steady and unsteady Euler solutions. At other positions not shown here, a deviation of the shock amplitude is also noticed. These deviations are drastically reduced when solving the RANS equations instead of the Euler ones for the propagation (in particular the shock angle issued from CFD is well recovered). This validates the chaining method and also shows that the viscosity plays a role on the propagation of shocks.

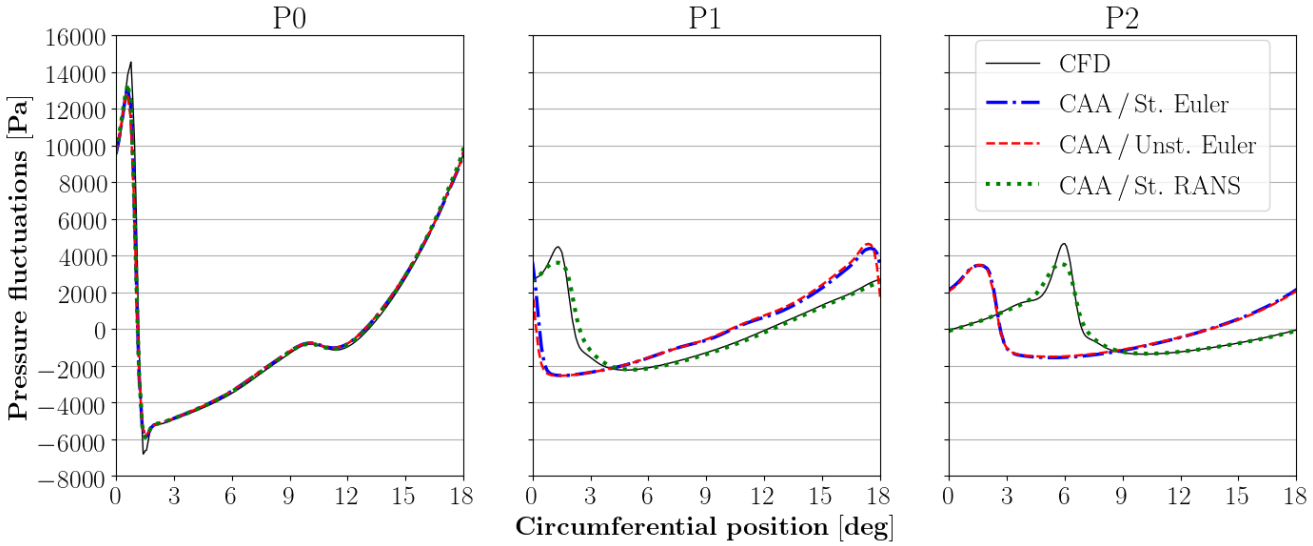

Figure 2: Azimuthal evolution of pressure fluctuations at 95 % of blade height on planes P0, P1 and P2.

5. In-duct acoustic results

The focus is now put on in-duct acoustic quantities. The acoustic power is first evaluated by integration over axial planes of the acoustic intensity derived using Cantrell & Hart's formula [13]. Its axial evolution at BPF1, BPF2 and BPF3 is given in Fig. 3 for all simulations. Note that the axial position is normalized by the length of the inlet duct, with zero being the injection plane location. In the region where the CFD solution is available (up to 0.24), there is a remarkable agreement between the CFD solution and the CAA solution with RANS model, which further validates the chaining strategy. Again, the CAA results obtained with steady and unsteady Euler simulations are quasi-identical. They match

the CFD and CAA/RANS results at BPF1 but they progressively deviate from them at BPF2 and BPF3, with local differences going up to 5 dB approximately. This shows that neglecting the viscosity tends to underestimate the acoustic energy carried by the shock waves, especially at high frequencies. We should however note that in all cases, the evolution of the acoustic power at BPF2 and BPF3 is unexpected. At BPF1, the non-linear region with power attenuation is clearly identified and goes up to 0.4. It is followed by a plateau which seems to indicate the transition to the linear region. A similar trend would have been expected at BPF2 and BPF3, but it appears that the power levels keep decreasing up to the inlet plane (with even a hump in the Euler solutions). No clear explanation of this behaviour has been found yet. Nevertheless, it should be noted that the total acoustic power (dominated by BPF1 levels) is effectively conserved in the linear region (from 0.4).

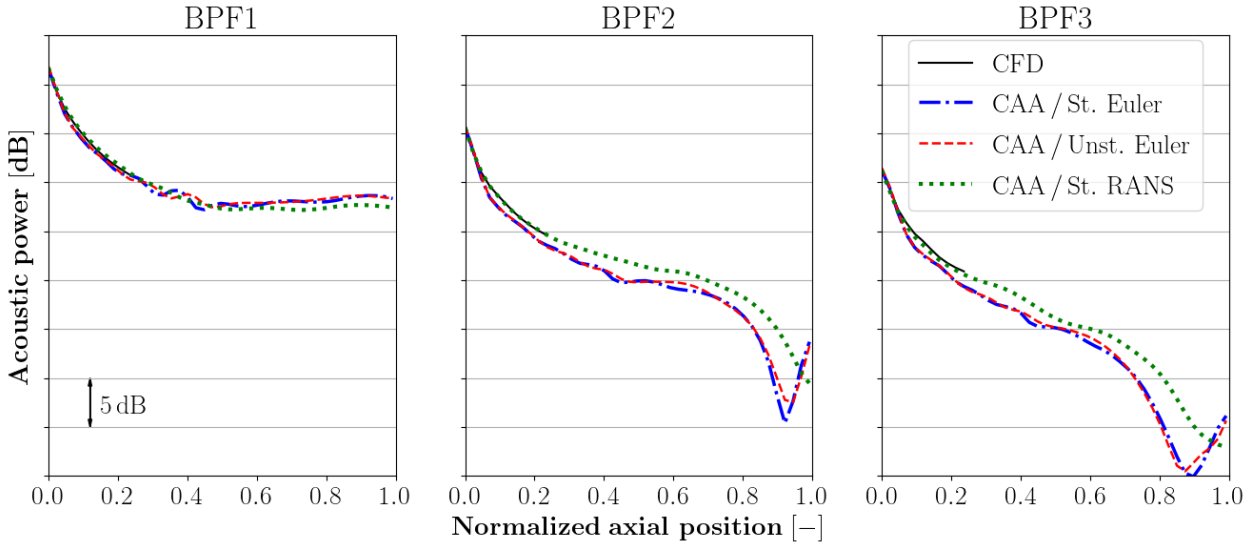

Figure 3: Axial evolution of in-duct acoustic power at BPF1, BPF2 and BPF3. The CFD solution is available up to 0.24.

In order to further analyze these results, the radial evolution of acoustic intensity (the integration of which gives the acoustic power) is given for the first three BPFs on plane P2 in Fig. 4. We observe again a very good agreement between the direct CFD results and the CAA results obtained by solving the RANS equations, proving one more time the consistency of the chaining methodology. The steady and unsteady Euler simulations give also similar results, but they differ importantly from the CFD and CAA/RANS results, especially at BPF2 and BPF3. In the latter simulations, there are strong intensity variations from 80% to 100% of blade height. These variations are not predicted in the Euler simulations where a Bessel shape is obtained in accordance with classical cylindrical duct acoustic theory (assuming inviscid flow).

6. Far-field acoustic results

Finally, the far-field radiation of shock waves is predicted using the Kirchhoff's integral method in the frequency domain implemented in ONERA's in-house *MIA* solver [14] using the source data extracted from the CAA simulations over the surface shown in red in Fig. 1. Note that the surface used does not completely enclose the nacelle in order not to account for the waves that go inside the absorbing walls of the real geometry. There is no more direct CFD results to compare with (as having a CFD simulation that goes up to the far-field is not affordable) so that the results are now evaluated against the experimental data acquired during the TurboNoiseBB project. The sound pressure level (SPL) directivities obtained

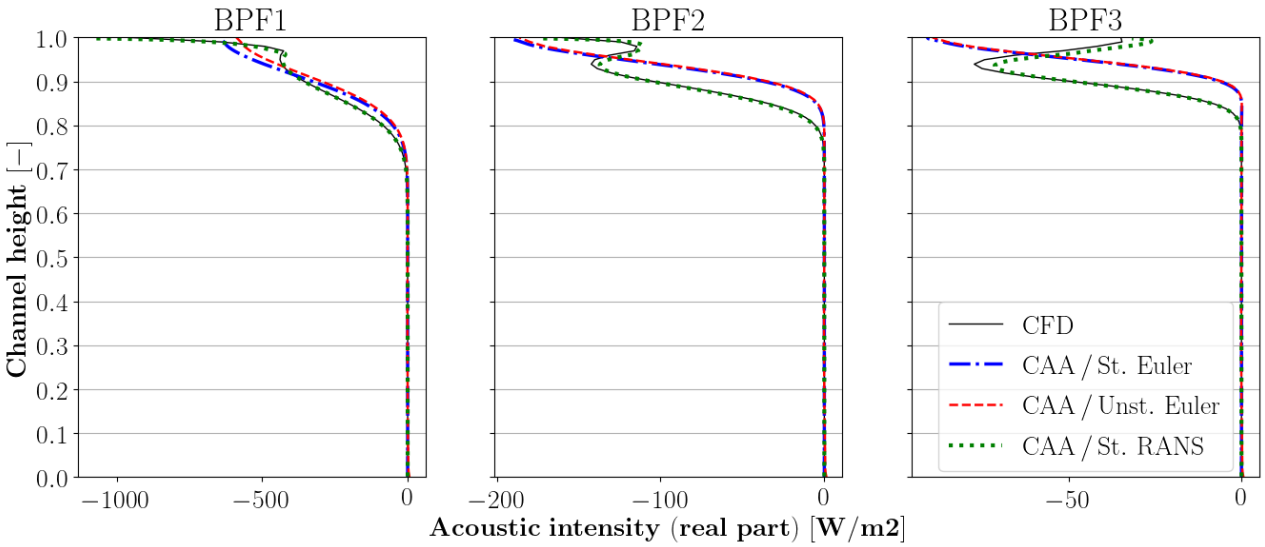

Figure 4: Radial profile of acoustic intensity at BPF1, BPF2 and BPF3 on plane P2.

at BPF1, BPF2 and BPF3 over the experimental far-field arc are given in Fig. 5. The 0 and 180 degrees angles correspond to the forward and to the backward positions respectively. For each BPF, two curves represent the experimental results: one curve (labeled "Exp.") is for the direct experimental result at the considered BPF while the other (labeled "Exp. with subharm.") also considers all its subharmonics (i.e. for BPFn, the rotation harmonics from $(n-1)B+1$ to nB are summed up). As the present numerical simulations do not include stagger variation between the blades, these subharmonics (or multiple pure tones) responsible for the buzz-saw noise cannot be predicted. We therefore consider the numerical results as satisfying if they are in-between these two experimental results. For all BPFs, the experimental noise levels are higher below 45 degrees, probably because of the presence of low-order modes caused by rotor-stator interaction (not included in the present simulations). And above 90 degrees, the simulations levels are generally higher, but the geometry modification (see Fig. 1) should play a role in this region. The rest of the discussion therefore focuses on the region from 45 to 90 degrees, where the sound emission is predominant. At BPF1, all the results are in reasonably good agreement in this region, which validates the full numerical methodology at the predominant frequency. The effect of viscosity is not significative at this frequency, as already noticed in the intensity profile analysis (see Fig. 4). At BPF2 and BPF3, the Euler results are surprisingly in better agreement than the CAA/RANS results with the experimental data. This is more visible at BPF2 where the CAA/RANS directivity displays a destructive interference around 65 degrees, contrary to all other results. There is no clear explanation of this behaviour, but it may be related to a higher sensitivity of the CAA/RANS results to the geometry modification of the nacelle.

Finally, the radiated power levels obtained by integration of the intensity evaluated on the far-field arc are given in Fig. 6 for the first three BPFs. For the numerical results, the bars show the power levels obtained with the Kirchhoff's integral method while the points show the in-duct power levels at inlet lip (normalized position of 1 in Fig. 3). The balance between the radiated and in-duct power levels is well respected, except at BPF3 where discrepancies up to 6 dB are observed (which is probably due to to an insufficient mesh resolution in the radial direction outside of the nacelle). Moreover, we observe an increasing impact of the multiple pure tones with the frequency (responsible of about a 3 dB difference at BPF1 and a 7 dB difference at BPF3). In the end, the predicted power levels are always in-between the two experimental results or close to one of them. This gives confidence in the presented results, especially at BPF1. Nevertheless, at BPF2 and BPF3, the important contribution of the multiple pure tones and the

unexpected directivity in the CAA/RANS results make difficult the interpretation of the results.

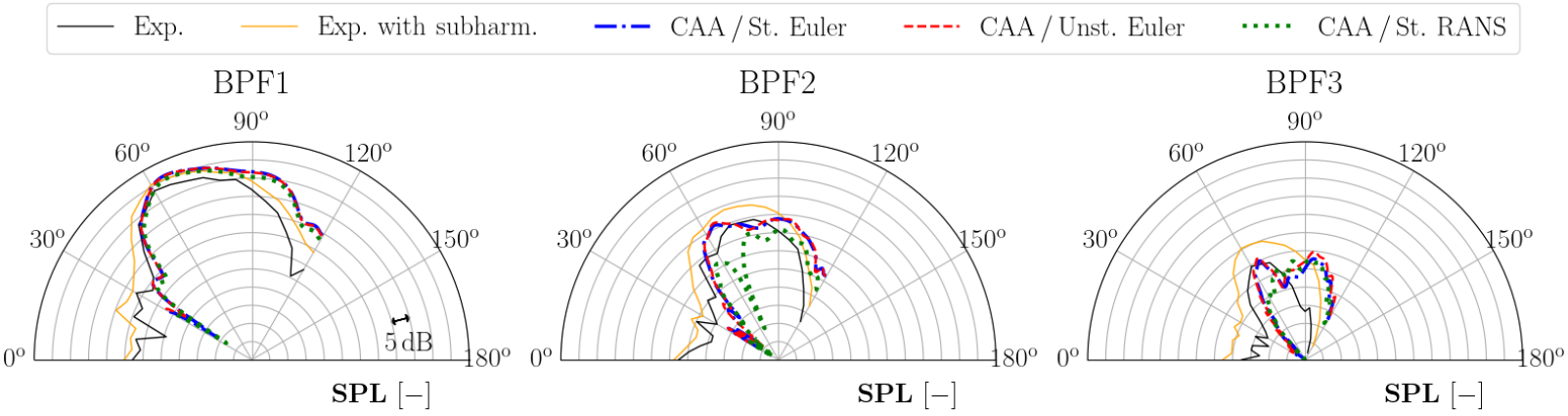

Figure 5: Far-field SPL directivity at BPF1, BPF2 and BPF3.

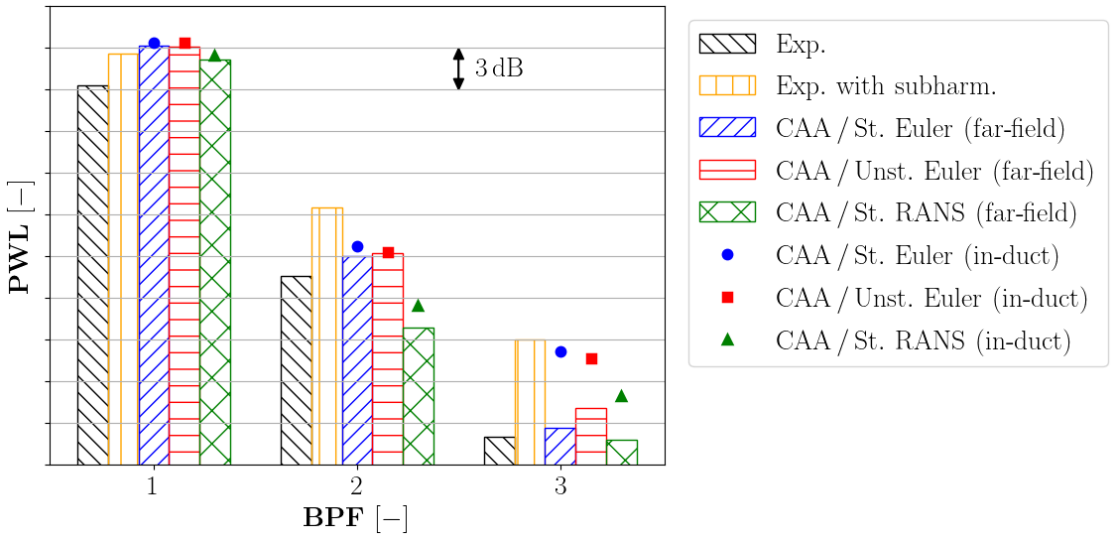

Figure 6: Far-field acoustic power balance.

7. Conclusion

This paper shows a further validation of a CFD/CAA chaining method to compute shock wave generation and propagation. A CFD simulation is first performed to compute the generation of shock waves, and a CAA simulation is then realized to compute its propagation. The shock characteristics extracted from the CFD simulation over an axial plane are specified into the CAA domain using a non-reflecting boundary condition. Up to now, this methodology had only been applied with the CAA simulation being performed by solving the unsteady Euler equations in the absolute frame. In this paper, a more complete evaluation of the methodology is proposed on the ACAT1 fan stage, for which experimental data are available, by testing several strategies for the CAA simulation. To this end, the propagation of shock waves has been done by solving 1/ the steady Euler equations in the relative frame, 2/ the unsteady Euler equations in the absolute frame, and 3/ the steady RANS equations in the relative frame. The results of each simulation has been evaluated against the direct CFD results and the experimental measurements.

The comparison with the direct CFD simulation has shown an excellent behaviour of the chaining strategy with a perfect recovering of the shock signature, acoustic intensity profiles and acoustic power when the CAA simulation is done by solving the RANS equations. On their side, the CAA simulations with steady and unsteady Euler equations give quasi-identical results, validating the use of the methodology even in the steady context when the configuration allows for the use of the time-azimuthal angle analogy. The effect of viscosity on in-duct acoustics has also been highlighted, with a modification of the shock angle, amplitude and shape and a modification of the intensity profile with a gathering of the energy close to the nacelle wall. As a result, the power levels predicted with the Euler simulations are slightly underestimated at the last position where the CFD solution is available.

The comparison with the experimental far-field results is however more difficult to interpret. Indeed, at BPF2 and BPF3, the geometry modification that has been made in the simulations to avoid having absorbing walls appears to affect the radiation patterns and the contribution of the multiple pure tones in the experimental data (not included in this work) is significant. However at BPF1, a very good agreement is obtained between all methods and the measurements, which at least validates the full methodology at the predominant frequency. It should be helpful to repeat the CAA simulations with the real geometry (even without absorbing walls) to see how the far-field radiation is impacted.

REFERENCES

1. Doherty, M. and Namgoong, H. Impact of Turbofan Intake Distortion on Fan Noise Propagation and Generation, *22nd AIAA/CEAS Aeroacoustics Conference*, no. 2016-2841, (2016).
2. Milidonis, K. F., Hynes, T., Doherty, M. and Namgoong, H. The Effect of Steady Intake Distortion on Fan MPT Noise Under Sideline Flight Conditions, *24th AIAA/CEAS Aeroacoustics Conference*, no. 2018-4188, (2018).
3. Winkler, J., Reimann, C. A., Reba, R. A. and Gilson, J. Turbofan Inlet Distortion Noise Prediction with a Hybrid CFD-CAA Approach, *20th AIAA/CEAS Aeroacoustics Conference*, no. 2014-3102, (2014).
4. Winkler, J., Reimann, C. A., Gumke, C. D., Ali, A. A. and Reba, R. A. Inlet and Aft Tonal Noise Predictions of a Full-Scale Turbofan Engine with Bifurcation and Inlet Distortion, *23rd AIAA/CEAS Aeroacoustics Conference*, no. 2017-3034, (2017).
5. Laban, M., Kok, J. C. and Brouwer, H. H. CFD/CAA Analysis of UHBR Engine Tonal Noise, *24th AIAA/CEAS Aeroacoustics Conference*, no. 2018-3780, (2018).
6. Daroukh, M., Polacsek, C. and Chelius, A. Shock Wave Generation and Radiation from a Turbofan Engine Under Flow Distortion, *AIAA Journal*, **58** (2), 787–801, (2020).
7. Thisse, J., Polacsek, C., Mayeur, J., Khelladi, S., Gloerfelt, X. and Lafitte, A. Numerical Simulations of Shock-Wave Propagation in Turbofan Intakes, *22nd AIAA/CEAS Aeroacoustics Conference*, no. 2016-2879, (2016).
8. Behn, M. and Tapken, U. Investigation of Sound Generation and Transmission Effects Through the ACAT1 Fan Stage using Compressed Sensing-based Mode Analysis, *25th AIAA/CEAS Aeroacoustics Conference*, no. 2019-2502, (2019).
9. Köhler, W. The Influence of the TCS on the Circumferential Mode Distribution in the Inlet of a Fanrig (UFFA), *Turbo Expo: Power for Land, Sea, and Air*, no. GT2012-69762, (2012).
10. Tapken, U., Bauers, R., Neuhaus, L., Humphreys, N., Wilson, A., Stoehr, C. and Beutke, M. A New Modular Fan Rig Noise Test and Radial Mode Detection Capability, *17th AIAA/CEAS Aeroacoustics Conference*, no. 2011-2897, (2011).
11. Cambier, L., Heib, S. and Plot, S. The Onera elsA CFD software: input from research and feedback from industry, *Mechanics & Industry*, **14** (3), 159–174, (2013).
12. Thompson, K. W. Time Dependent Boundary Conditions for Hyperbolic Systems, *Journal of Computational Physics*, **68** (1), 1–24, (1987).
13. Cantrell, R. H. and Hart, R. W. Interaction between Sound and Flow in Acoustic Cavities: Mass, Momentum, and Energy Considerations, *The Journal of the Acoustical Society of America*, **36** (4), 697–706, (1964).
14. Polacsek, C., Burguburu, S., Redonnet, S. and Terracol, M. Numerical Simulations of Fan Interaction Noise using a Hybrid Approach, *AIAA Journal*, **44** (6), 1188–1196, (2006).